RC23081 (W0401-120) January 26, 2004
Materials Science

IBM Research Report

Surface Potential and Morphology Issues of Annealed $(HfO_2)_x(SiO_2)_{1-x}$ Gate Oxides

R. Ludeke[1], P. Lysaght[2], E. Cartier[1], E. Gusev[1], M. Chudzik[3], B. Foran[3], G. Bersuker[2]

[1]IBM Research Division
Thomas J. Watson Research Center
P.O. Box 218
Yorktown Heights, NY 10598

[2]International Sematech
2706 Montopolis Drive
Austin, TX 78741

[3]IBM Microelectronics Division
Hopewell Junction, NY 12533

Research Division
Almaden - Austin - Beijing - Haifa - India - T. J. Watson - Tokyo - Zurich

Surface Potential and Morphology Issues of Annealed $(HfO_2)_x(SiO_2)_{1-x}$ Gate Oxides

R. Ludeke[1], P. Lysaght[2], E. Cartier[1],E. Gusev[1], M. Chudzik,[3] B. Foran[3] and G. Bersuker[2]
[1]IBM T. J. Watson Research Center, P. O. Box 218 Yorktown Heights, NY 10598
[2]International Sematech, 2706 Montopolis Drive, Austin, TX 78741
[3]IBM Microelectronic Division, Hopewell Junction, NY, 12533

Abstract. The surface morphology and surface potential variations of annealed $(HfO_2)_x(SiO_2)_{1-x}$ films were investigated by non-contact Atomic Force Microscopy (NC-AFM) in ultra high vacuum. Additional modes of data acquisition included contact potential difference (CPD) and differential capacitance. Two types of samples were investigated. The first, a set consisting of 4 nm thick samples with HfO_2 compositions of x=0.4, 0.6 and 0.8, were annealed at 1000° C for 10 sec. in N_2 gas. The second, a 2.2 nm thick sample of composition $(HfO_2)_{0.78}(SiO_2)_{0.22}$ was annealed in vacuum at 50° C intervals from 850-1000° C. The anneals resulted in a microstructure consisting of phase-separated HfO_2 crystallites and amorphous silica, as observed in high resolution transmission electron microscope (HRTEM) images. The crystallites appear to be responsible for most of the morphology observed with the AFM, with surface features for the hafnium rich x=0.6 and 0.8 compositions generally agreeing with the crystal sizes observed by HRTEM. The AFM images for the x=0.4 sample showed substantially broader features than the 5 nm crystallites seen by HRTEM. The AFM results suggest that the surface was largely covered with a low dielectric constant (κ) material, presumably silica, which shrouded details of the bulk microstructure. The vacuum annealed sample showed an initial trend to lower roughness and CPD fluctuation range, with a minimum in both (rms roughness =0.077 nm and ΔCPD=0.2 V) for a 10 second anneal at 900°C. Thereafter both measures increased substantially. The 1000° C vacuum annealed sample compared favorably in structure, roughness, and to lesser extent in the CPD fluctuation range with the 1000° C N_2 annealed sample. The N_2 annealed samples for x=0.4 and x=0.8 exhibited CPD fluctuations as large as 0.4 V, with a smaller value of 0.22 V observed for the x=0.6 sample. CPD fluctuations consist of a small amplitude substructure that correlated with the micro-structural features of the surface, superimposed on longer range CPD fluctuations (20 to >50 nm) unrelated to any surface features. Their origin is speculative, but could be associated with bulk and/or interface fluctuations in the density of trapped charge. Their potential adverse impact on device performance is discussed.

I. Introduction.

A limiting factor for future use of the ubiquitous SiO_2 gate oxides is the increase in electron tunneling that results from scaling devices to lower dimensions.[1] Suppression of the leakage current is thus the objective of an extensive search for a suitable high dielectric constant (κ) substitute for SiO_2,[2-3] the higher κ allowing a thicker gate dielectric that reduces tunneling while maintaining the electric fields necessary for controlling the channel current. Issues of compatibility with Si vis-à-vis their thermal stability has limited the choices,[2,4] with the binary Zr and Hf oxides and their alloys with SiO_2 and Al_2O_3 being the primary candidates today.[2,5-9] Even though seemingly acceptable from a macro-chemical point of view, all high-κ materials and their interfaces with Si still exhibit electrically active defects of concentrations deemed unsuitably high for acceptable device performance, including device reliability.[10-12] However, a successful incorporation of high-k gate oxides in future generations of integrated circuits depends not only on reduction and control of gate leakage currents and interface states, but on issues relating to carrier control and carrier mobility in the channel. These issues in turn are affected by certain extrinsic properties of the gate dielectric, such as interface roughness, oxide charge and possibly by workfunction fluctuations due to compositional disorder or multifaceted polycrystalline orientations. Amorphous phases, in analogy to the standard SiO_2 thermal oxides, are expected to prevent or minimize such problems, in addition to avoiding detrimental grain boundary effects during device processing, such as diffusion.[9] However, crystallization may be an unavoidable consequence of the high temperature processing required for the polysilicon gate metallurgy, a process that could also lead to undesirable phase separation of the gate oxide components. The latter has now been well documented for rapid thermal anneals of thin films of $(HfO_2)_x(SiO_2)_{1-x}$ and $(ZrO_2)_x(SiO_2)_{1-x}$, with no evidence for the existence of a crystalline silicate phase predicted by equilibrium phase diagrams.[6,13-15] For $(HfO_2)_x(SiO_2)_{1-x}$ films two different, composition-dependent microstructures of the phase separated material have been reported,[13,15] an amorphous phase characteristic of spinodal decomposition for low HfO_2 content (x=0.4), and a nucleated phase of crystalline HfO_2 embedded in an amorphous, silica-rich matrix for x=0.8.

The investigations of the $(HfO_2)_x(SiO_2)_{1-x}$ and $(ZrO_2)_x(SiO_2)_{1-x}$ films have primarily focused on the compositional and structural characteristics of the phase separated alloy films using X-ray mediated techniques, high resolution transmission electron microscopy (HRTEM) and far infrared spectroscopy.[6,13-15] However, little is known of the surface morphology or roughness and of surface potential fluctuations that result from the phase change, as substantial variations in both, in comparison to SiO_2 gate dielectrics, may prove detrimental to device performance and/or reliability. We have performed and report here atomic force microscope (AFM) studies of the surface topography and surface potential variations of thin film samples of the $(HfO_2)_x(SiO_2)_{1-x}$ system annealed ex-situ in N_2 gas, two of which were cut from the identical lot as the samples used in prior X-ray studies.[13,15] As there were issues regarding the evolution of the film characteristics for intermediate annealing temperatures, we also performed in-situ vacuum anneals of a $(HfO_2)_{0.78}(SiO_2)_{0.22}$ sample, which was grown just prior to the vacuum AFM studies.

II. Experimental Details.

A. AFM basics

We will digress here to discuss briefly the AFM and the physical principles underlying the measurements, as these have not been previously applied to high-κ dielectric materials. The AFM is a JEOL JSPM-4500A ultra high vacuum (UHV) instrument operating at a base pressure of 10^{-8} Pa ($\sim 1\times10^{-10}$ torr). The non-contact AFM (NC-AFM) operating mode was used

exclusively, in which the AFM cantilever oscillates near its resonance frequency ω_o with the cantilever tip just a couple of nanometer from the surface. At this proximity the tip senses the repulsive force field F(z) of the surface atoms, where z is the surface normal. The interaction between cantilever tip and surface is through the force gradient $F' \equiv \partial F_z/\partial z$, which modifies the cantilever resonance frequency by $\delta\omega = \delta F' \omega_o/2k$. $\delta F'$ is the change in the force gradient normal to the surface arising from changes in the tip-surface interaction,[16] and k is the cantilever stiffness. Thus $\delta\omega$ is a direct measure of $\delta F'$. The AFM operates in the constant $\delta\omega$ mode, with changes detected by frequency demodulation methods.[16] A feedback system, as illustrated in Fig.1, adjusts the extension of the z-piezo to maintain constant $\delta\omega$ during the X-Y scans generated with the piezo-electric scanner.

The cantilever resonance frequency is affected as well by other forces exerted on the tip. Of primary importance here are electrostatic forces F_e arising from differences in the workfunctions between sample and tip, specifically the contact potential difference or CPD. Electrostatic forces can also arise from charges in the sample or from an external voltage V_{ext} applied between the sample and tip. The force gradient $\partial F_e/\partial z$ of this interaction is added to that of the tip-surface interaction, with the feedback responding to the combined force gradients. V_{ext}, which is referenced here to the tip, takes the form of a dc bias V_b added to a low frequency (1 kHz) ac voltage: $V_{ext} = V_b + V_{ac}\sin\omega_p t$. The force gradient takes the form:[17]

$$\partial F_e/\partial z = \tfrac{1}{2}V^2 (\partial^2 C_{eff}/\partial z^2) + \partial F_q(V_{ext})/\partial z = \tfrac{1}{2} [V_b + V_{CPD} + V_{ac}\sin\omega_p t\,]^2(\partial^2 C_{eff}/\partial z^2) + \partial F_q(V_{ext})/\partial z \quad (1a)$$

$$\partial F_e/\partial z \equiv F_e'(z) = F_{dc}' + F_e'(\omega_p) + F_e'(2\omega_p). \quad (1b)$$

Ignoring the dc term, the frequency dependent terms are:

$$F_e'(\omega_p) = (\partial^2 C_{eff}/\partial z^2)\,[V_b + V_{CPD}]V_{ac}\sin\omega_p t + \partial F_q(\omega_p)/\partial z \quad (2)$$

and

$$F_e'(2\omega_p) = \tfrac{1}{4}(\partial^2 C_{eff}/\partial z^2) V_{ac}^2 \cos(2\omega_p t). \quad (3)$$

The $\partial F_q(V_{ext})/\partial z$ term arises from the interaction of V_{ext} with a localized charge q embedded in the dielectric sample with dielectric constant κ. For a spherical tip of radius r and at a distance $\mathbf{d} = z\,\hat{z} + l\,\hat{l}$ from the center to the charge, the force gradient is given by

$$\partial F_q(V_{ext})/\partial z = (qV_{ext} r/\varepsilon_{eff})[(l^2 - 2z^2)/(z^2 + l^2)^{5/2}], \quad (4)$$

where l is the lateral distance from the tip apex to the charge and $\varepsilon_{eff} = (\kappa+1)/2$. In eqs. (1-3), C_{eff} is the effective capacitance between cantilever and sample. Although C_{eff} depends on the sample-cantilever geometry, in the present experiments most of the contributions to C_{eff} come from the tip-surface interaction because of their close proximity. If κ and/or the substrate doping concentration fluctuates laterally, C_{eff} will vary as well across the surface. Doping fluctuations will modify the depletion width, but this effect is of little relevance here because of the homogeneously doped Si samples used throughout the experiments. A signal proportional to the fundamental harmonic term (2) is obtained by feeding the demodulated output of the phase-locked amplifier of the AFM detector into a lock-in amplifier tuned at ω_p. The output, which is proportional to $V_b + V_{CPD}$, can be used to generate contrast for a second image that is acquired concurrently with the topography.[18] The output of the lock-in amplifier can also be compared to a reference, usually 0, and the "error" converted to a variable V_b, which is fed back to maintain zero lock-in output; that is $V_b + V_{CPD} = 0$, with V_b corresponding to the negative of the contact potential difference. This feedback loop is illustrated as well in Fig. 1. Contrast in the second

image is then generated with the V_b signal. We term such an image the CPD image. It should be noted that in this mode variations in C_{eff}, should they exist because of fluctuations in κ for instance, do not affect image contrast and are therefore not observed in the CPD image. Since the phase of the lock-in output is arbitrary, we adopt the convention that a low CPD signal, giving rise to dark areas in the image, corresponds to an increase in the local workfunction.

The AFM detector output can also be fed into a second lock-in amplifier tuned to $2\omega_p$, as shown in the top right of Fig. 1. Its output is then proportional to the second harmonic term $F_e'(2\omega_p)$, eq. (3), which contains only contributions from the differential capacitance term $\partial^2 C_{eff}/\partial z^2$. Thus a third image generated with this signal represents the contribution of C_{eff}. It can be shown that for a model tip of spherical symmetry in the immediate vicinity of a planar dielectric medium,[19]

$$\partial^2 C_{eff}/\partial z^2 = 4\pi\varepsilon_o r\{[(\kappa-1)/(\kappa+1)]r/z^3 + [(\kappa-1)/(\kappa+1)]^2 r^2[(96z^2+8r^2)/(4z^2-r^2)^3] + ...\} \quad (5)$$

where r is the radius of the spherical tip, z the distance from the tip's center to the sample surface and ε_o the permittivity. One of our earlier goals was an assessment of fluctuations in κ arising from heterogeneity in the composition of the films by measuring changes in $\partial^2 C_{eff}/\partial z^2$ ($\equiv \delta C''_{eff}$). It is readily shown, however, that a change in the differential capacitance $\delta C''_{eff}$ due to a change δκ is given by $\delta C''_{eff} / C''_{eff} \propto \delta\kappa/(\kappa^2-1)$,[19] which implies that for high κ dielectrics ($\kappa \gtrsim 10$) even modest changes of 10-20% in κ have negligible effect (<1%) on the differential capacitance. Together with the additional ¼ prefactor in eq. 3 renders the differential capacitance signal rather small for conventionally used values of V_{ac} (< 1 volt). Since surface roughness results in localized changes in the thickness t of the dielectric, such roughness can induce changes in the capacitance, which are $\propto -\delta t/(\kappa g+t)$, where g corresponds to the effective tip-sample separation (~2 nm). Thus thickness fluctuations are attenuated only to the inverse first order in κ and are expected to be dominant for high κ materials. This was borne out in our (unpublished) differential capacitance images, although for the smoothest high-κ layers a κ-dependence was observed to correlate with microstructure in the topography.[19]

B. Sample preparation.

The $(HfO_2)_x(SiO_2)_{1-x}$ samples, of ≈4 nm thickness and compositions x=0.4, 0.6 and 0.8, were deposited by metalorganic chemical vapor deposition (MOCVD) on HF-last treated Si(100) substrates. The as-grown alloy films were amorphous. After deposition the samples were annealed for 10 seconds at 1000° C in N_2 gas and subsequently shipped from Sematech to IBM. Once received by us, the samples were cleaved into smaller 7×1.5 mm^2 pieces suitable for AFM investigations. Aside from spraying the sample with a clean N_2 jet no additional cleaning treatments were performed. The samples were placed in the preparation chamber of the UHV system and were heated to 300-400° C in vacuum of < 10^{-7} Pa (<10^{-9} torr) for several hours to remove volatile components. This procedure has been found in the past to leave surfaces virtually free of measurable particulate contaminants. After cooling to room temperature the samples were transferred in UHV into the AFM analysis chamber for the measurements.

The sample for the vacuum annealing experiments was cleaved from a 2.2 nm thick $(HfO_2)_{0.78}(SiO_2)_{0.22}$ layer grown as well by MOCVD on a Si(100) wafer, which was covered with a thin, 0.8 nm SiO_2 layer. The as-grown layer was amorphous. The sample was transferred with minimal ambient exposure to the AFM system. It was subsequently outgassed at ~300° C for several hours in UHV to assure the removal of volatile surface contaminants adsorbed during the brief transport period. After an initial AFM measurement in the as-grown condition, the sample

was sequentially annealed for 10 seconds in UHV at temperature intervals of 50° C starting at 850° C. Two final anneals for 10 and 15 seconds (for a total 25 seconds) were made at 1000° C. The temperature was measured over a sampling spot size of <1 mm with an Impac® IR pyrometer optimized in the 1.45-1.8 μm wavelength range. The estimated error was ±10° C. AFM measurements were made between the anneals and after the sample reached room temperature. Heating of the sample was accomplished by passing a dc current lengthwise through the sample. The small sample size allowed rapid and controlled changes in temperature in the high temperature ranges (>500° C).

III. Topography and surface potential measurements.

A. N_2 annealed $(HfO_2)_x(SiO_2)_{1-x}$ Layers

As reference for the AFM studies, we show in Fig. 2 some prior results of the structure of the 1000° C/10s annealed films, specifically plan view HRTEM images of the x=0.4, 0.6 and 0.8 compositions.[13,15] Fig. 2a depicts the TEM image of the silica-rich x=0.4 sample, a composition that lies in the high temperature miscibility gap of the hafnia-silica phase diagram. The image reveals the pattern of a microstructure formed by spinodal decomposition from the thermodynamically unstable amorphous phase.[13] The crystalline phase, with typical dimensions of ~5 nm for the stated annealing conditions, is believed to be tetragonal HfO_2 embedded in a silica-rich amorphous phase.[20] For HfO_2-rich alloys, such as x=0.6 and x=0.8, the composition is outside the miscibility gap at the annealing temperature and the rapid thermal anneal results in a different microstructure, such as shown for the stated compositions in Fig. 2b and 2c. The microstructure in both images is similar except for the crystallite sizes, and is attributed to a phase separation proceeding by nucleation and growth of HfO_2 crystallites.[13,15] The grains for the x=0.6 composition remain in the 5 nm size range, but exhibit a more regular rounder shape than those for the x=0.4 compositions. The grain sizes definitely increase for the x=0.8 composition, with averages in the 10 nm range, but some exhibiting substantially larger dimensions. Prolonged high temperature anneals increase the grain size further.[13] For the x=0.8 composition the crystalline phase has been identified as monoclinic and tetragonal HfO_2.[15]

The topography obtained in the NC-AFM mode and the simultaneously acquired CPD image of the ~4 nm thick annealed $(HfO_2)_{0.4}(SiO_2)_{0.6}$ sample is shown in Fig. 3. The image scale of 200×200 nm^2 is considerably larger than that for the HRTEM images in Fig. 2. A better assessment of the size range of the microstructure can be obtained from the height profiles along the dashed lines, shown in Fig. 3c. It becomes immediately apparent that the scale of features in the AFM image ranges from ~8 to 20 nm in extent, a factor of 2-4 larger than those seen in the HRTEM image Fig, 2a. The latter, essentially a bulk view, is largely insensitive to surface morphology and surface composition and therefore conclusions inferred from the HRTEM pictures are not necessarily in contradiction with AFM images. The latter indicates that at least the coarser features of the surface morphology are composed of aggregates of the bulk microstructure. The CPD image, Fig. 3b, shows even less detail than the topography, suggesting that the outer surface layer is fairly homogeneous. A prominent feature in the CPD image and in the profile is the bright protrusion located at the center of the cut. Its counterpart in the topography is a small dark area that images as a depression or hole. It is one of the very few features in the image and the only feature in both profiles that correlate exactly in position. The "hole" together with its spatial correlation to a prominent feature in the CPD image strongly suggests that its origin derives from charge trapped in the dielectric. Our past work on SiO_2 has shown that even a single electron trapped near the surface appears as a nanometer sized "hole" in topography.[18] The more positive (bright) value for this feature in CPD, with reference of polarity relative to the tip, indicates that the charge is negative. If indeed the image feature is caused by

trapped charge, and we are reasonably sure of it, its prominent signature in the CPD image implies that it has to be imbedded in a low κ material, such as a thin silica layer, as observed in the bulk. A high-κ material, as we have recently shown,[19] would drastically suppress trapped charge contributions to the CPD signal. It is thus quite likely that a low κ material, most likely amorphous silica, is the dominant constituent of the outer layer, which is consistent with the featureless CPD image, the presence of a weakly screened trapped charge and prior work showing the abundance of this phase throughout the bulk of the SiO_2-rich sample. [13,15]

We turn next to the NC-AFM images of the more Hf-rich (x=0.6) sample, shown in Fig. 4. Its topographic features appear to be more detailed than those of the just discussed x=0.4 sample. Features range in size from about 6 to 15 nm, within range of the values seen in Fig. 2b for the HRTEM results. A significant difference between the x=0.4 and x=0.6 annealed samples can be seen in the CPD images. Comparing Figs. 3b and 4b, a richer substructure is immediately apparent in the latter, indicating a more complex surface potential composition, which seems to reflect a greater heterogeneity of the chemical composition of the surface. This point is emphasized when one compares topography and CPD profiles, which are shown in Fig. 4c. Close inspection of the two profiles reveals another major difference between the two compositions: whereas those for the x=0.4 composition showed only one profile feature spatially correlated between the two profiles, every significant peak in the topography profile of Fig. 4c corresponds to a peak in the CPD profile. It should be pointed out that the enhanced details in this and later images and profiles is repeatable structure. Its appearance here cannot be attributed to better instrumental resolution, as the identical cantilever was used for all three compositions, with data collected in the order presented here.

Additional changes are observed in the images for the annealed sample with the highest HfO_2 content, shown in Fig. 5. The topography consists of a coarse nodular structure in the size range of 10-25 nm that in turn contains a nodular substructure in the 5-10 nm range. It is thus somewhat larger than that of the x=0.6 sample, but in qualitative agreement with the HRTEM observations. The substructure is more discernable in the CPD profile of Fig. 5c. As for the previous sample, virtually all peaks in the CPD profile match peaks, including shoulders and minor peaks in the topography profile, a noted exception being the prominent structure just below the 50 nm position in the profile, whose origin could be due to trapped negative charge. This assignment is more tentative than a similar feature for the x=0.4 sample in Fig. 3. Its prominence here is a bit suspect because of the predominance of the high-κ Hf-rich composition of this sample, although the extent of the CPD change of the feature in question in Fig. 5c is only 1/3 of that in Fig. 3c.

B. Vacuum annealed $(HfO_2)_{0.78}(SiO_2)_{0.22}$

Vacuum annealing of a hafnium rich $(HfO_2)_{0.78}(SiO_2)_{0.22}$ layer was undertaken to study the evolution of film characteristics for intermediate annealing temperatures, as well as to assess possible differences arising from sample preparation and handling. One of the major differences between the two Hf-rich samples is the thickness, namely 2.2 nm compared to the 4 nm discussed above. After outgassing the sample in UHV at a temperature of ~300° C, topography and CPD images were taken. These "as-grown" images are shown in the upper left of Fig. 6; the topography is the topmost image, with the CPD image immediately below it. Profiles along cuts of the images are shown elsewhere;[19] it suffices to say here that virtually no correlation between features in the two images were observed. The image roughness measured over the 200×200 nm^2 images, as well as the range of the CPD over the image (lowest to highest value) is shown in Figs. 7 (a) and (b), respectively, as the leftmost data points. The first high temperature anneal was for 10 seconds at 850° C, a value above the crystallization temperature for the Hf-rich composition.[8,13] The topography and CPD images are shown as the top center pair in Fig. 6, as are

the remaining sets for the subsequent annealing steps at 900° C to 1000° C. A gradual coarsening of the topography is observed, which dramatically changes at 1000° C, especially after a second, 25 sec. anneal, shown in the last image set of Fig. 6. The coarse granular structure in this image is attributed to the formation of a HfSi or $HfSi_2$ phase, similar to what has been observed for uncapped ZrO_2-SiON stacks.[14] The corresponding CPD image, in the lower right of Fig. 6, indicates an excellent correlation with the topography; however the CPD contrast variations among the grains also suggests compositional variety among them.[19] The evolution of the coarsening of the surface is indicated in Fig. 7a, where both the image-wide mean and rms roughness are displayed. The roughness reaches a minimum for the 900° C anneal, which nearly coincides with the minimum in the CPD and in the image-wide CPD spread, shown in Fig. 7b. These trends suggest that the layer has reached a state of optimal morphological and electrostatic homogeneity. It remains to be seen if other alloy compositions and/or other properties, such as trap densities and dielectric constant, are optimized as well under these or similar annealing conditions. Roughness of the surface morphology and the CPD and its spread increase beyond the 900° C anneal. The abrupt change in CPD between the 10 and 25 second anneals at 1000° C indicates that the onset of silicide formation is abrupt and suggests that the silicide phase has not yet formed after the first 10 sec. anneal. A closer inspection of the images of the first 1000°C anneal may lend support to this assertion. An enlarged view of the topography and the CPD image, together with their profiles along a representative cut in the images is shown in Fig. 8. The nodular surface features range from ~8 to 20 nm in diameter, in excellent agreement with the size spread of the x=0.8 sample of Fig. 5. The average and rms roughness of the topographic images Fig. 5a and Fig 8a are also very similar. The fine structure in the CPD profile of Fig. 8 is well resolved. Detailed inspection reveals that similar to the correlation found in the hafnium-rich samples for x=0.6 and x= 0.8, the peaks in the topography profile overwhelmingly match those in the CPD profile. We can conclude form these observations that the 10 sec., 1000° C anneals in N_2 and vacuum lead to very similar morphologies and CPD characteristic for the two ≈80% HfO_2 samples. This conclusion also supports our prior stipulation that the formation of the Hf-silicide phase had not been initiated during the 10-second vacuum anneal.

IV. Concluding observations.

The topographic images of the N_2-annealed $(HfO_2)_x(SiO_2)_{1-x}$ (x=0.4,0.6 and 0.8) samples yielded values for the rms surface roughness of 0.201, 0.236 and 0.274 nm for the three compositions, respectively. These values are a factor of two larger than the rms roughness for both SiO_2-based gate oxides and ALD-grown HfO_2 layers of equivalent electrical thickness measured in the same way and for identical image areas.[19] Comparing the two Hf-rich samples, the 1000° C vacuum annealed $(HfO_2)_{0.78}(SiO_2)_{0.22}$ exhibited a very similar microstructure and correlative behavior with the CPD. However its rms roughness was a somewhat smaller 0.228 nm, which may still be of questionable use in devices. The modest improvement for the vacuum annealed sample may be due the lower film thickness, although other differentiating factors such as annealing environment and growth chemistry may contribute as well. A substantial improvements in the roughness was observed for a reduced annealing temperature of 900° C, for which the rms roughness of the $(HfO_2)_{0.78}(SiO_2)_{0.22}$ sample was a mere 0.077 nm.

CPD fluctuations were observed to have a local or fine structure component, which for the Hf-rich samples annealed at higher temperatures correlated with the microstructure. In addition long-range fluctuation (25 to >50 nm in extent) were observed that did not correlate with the topography. Consequently their origin appears to be bulk related, with fluctuations in bulk or interface trap densities a likely candidate. Variations in CPD among the annealed samples exhibited a somewhat different trend than the roughness trends. For the N_2 annealed samples, the x=0.6 sample exhibited a substantially lower value of 0.22 V compared to 0.49 and 0.44 V for the

x=0.4 and x=0.8 samples, respectively. In contrast the vacuum annealed $(HfO_2)_{0.78}(SiO_2)_{0.22}$ exhibited a CPD range of 0.30 V for the 1000° C anneal, which improved further to a value of only 0.21 V for the 900° C anneal. The 0.2 V value is in the range of CPD fluctuations observed for ALD-grown and annealed HfO_2 layers, as well as for SiO_2 layers not annealed in forming gas.[19] However, even 0.2 V fluctuations may be detrimental for device operation, depending to a large degree on the lateral extent of the fluctuations.[21] Potential fluctuations will scatter electrons, which will cause a decrease in their mobility. The scattering will be most intense when changes in the potential occur over dimensions comparable to the electron wavelength λ (λ=1.2 nm for an electron with kinetic energy of 1 eV). Fluctuation of such short scale, however, were not observed. A second detrimental effect of potential fluctuations can occur if their length scale is comparable to the device channel length. This situation is shown schematically in Fig. 9, where we superimpose an outline of a hypothetical device channel over an actual CPD image, specifically that taken of the x=0.8 $(HfO_2)_x(SiO_2)_{1-x}$ sample. Within the outlined channel boundary bands of substantially different potential values bridge the channel, which would cause portions of the channel to turn on or off before others, clearly an undesirable situation. Albeit a "worst" case scenario, only complete modeling of a realistic device would give insights as to the upper limit of CPD fluctuations and their lateral extent for acceptable performance.

We would like to make some final comments on the significance of the CPD measurements. It was generally observed for the higher temperature anneals that maxima in the CPD profiles matched in position those in the topography, as did the minima with the troughs in the topography. The same was observed for annealed HfO_2 layers.[19] However, occasionally the opposite was observed, as shown by the peak marked A in Fig. 8c, where the peak in the topography profile matches the trough or lower CPD value. This anticorrelation was observed more frequently for the lower annealing steps. The significance of such correlative relationship between topography and CPD is not presently known. That is, although we suspect the nodules to be primarily composed of HfO_2 for the Hf-rich alloys, CPD differences at present can neither corroborate nor dispute this point. The overall sign and magnitude of the CPD images is largely dependent on the substrate type and doping level. The other type of CPD fluctuations observed in most images, namely long-ranged changes discussed above in connection with Fig. 9, are particularly worrisome. Their origin remains unknown, but could derive from inhomogeneous distributions of charge trapped in the dielectric layer or at the Si interface.[22]

Acknowledgements The authors would like to thank Max Fischetti and Matt Copel for helpful discussions.

References

1. D. A. Buchanan, IBM J. Res. Dev**. 43,** 245 (1999).
2. G. D. Wilk, R. M. Wallace, J. M. Anthony, J.Appl.Phys., **89**, 5243 (2001).
3. M. L. Green, E.P. Gusev, R. Degrave, and E. Garfunkel, J. Appl. Phys. **90**, 2057 (2001).
4. K. J. Hubbard and D. G. Schlom, J. Mat. Res. **11**, 2757 (1996).
5. K. Kukli, M. Ritala, J. Sundqvist, J. Aarik, J. Lu , T. Sajavaara, M. Leskelä and A. Hårsta, J. Appl. Phys.**92**, 5698 (2002).
6. G. B. Rayner, Jr., D. Kang, and G. Lucovsky , J. Vac. Ssci. Technol. B **21**, 1783 (2003).
7. A. Callegari, E. Cartier, M. Gribelyuk, H. F. Okorn-Schmidt and T. Zabel, J. Appl. Phys. **90**, 6466 (2001).
8. D. A. Neumayer and E. Cartier, J. Appl. Phys. **90**, 1801 (2001).
9. M.-Y. Ho, H. Gong, G. D. Wilk, B. W. Bush, M. L. Green, W. H. Lin, A. See, S. K. Lahiri, M. E. Loomans, P. I. Räisänen and T. Gustafsson, Appl. Phys. Lett. **81**, 4218 (2002).
10. S. Zafar, A. Callegari, E. P. Gusev, and M.V. Fischetti, J. Applied Physics **93**, 9298 (2003).
11. M. Houssa, M. Naili, M. M. Heyns and A. Stesmans, J. App. Phys. **89**, 792 (2001).
12. A. Kumar, T.H. Ning, M.V. Fischetti and E. P. Gusev, J. Appl. Phys. **94**, 1728 (2003).
13. S. Ramanathan, P. C. McIntyre, J. Luning, P. S. Lysaght, Y. Yang, Z. Chen and S. Stemmer**,** J. Electrochem. Soc. **150,** F173 (2003).
14. M. A. Gribelyuk, A. Callegari, E. P. Gusev. M. Copel and D. A. Buchanan, J. Appl. Phys. **92**, 1232 (2002).
15. S. Stemmer, Y. Li, B. Foran, P. S. Lysaght, S. K. Streiffer, P. Fuoss and S. Seifert, Appl. Phys. Lett. **83**, 3141 (2003).
16. T. R. Albrecht, P. Grütter, D. Horne and D. Rugar, J. Appl. Phys. 69, 668 (1991).
17. M. Nonnenmacher, M. P. O'Boyle and H. K. Wickramasinghe, Appl. Phys. Lett. **58**, 2921 (1991).
18. R. Ludeke, J. Non-crystalline Solids, 303, 150 (2002).
19. R. Ludeke and E. Gusev, submitted to J. Appl. Phys.
20. S. Stemmer, Z. Chen, C. Levi, P. S. Lysaght, B. Foran, J. A. Gisby and J. R. Taylor, Jpn. J. Appl. Phys., Part 1, 42,3593 (2003).
21. M. Fischetti, private communications.
22. The potential at a position z above the surface due to a sheet charge σ buried a distance d below the surface of a dielectric medium is given by $\varphi=4\pi\sigma(d+z)/(\kappa+1)$. A potential change of 0.1 V at z=2 nm (the tip-sample distance) corresponds to a change in charge density of 1.5×10^{12} $|e|$ cm^{-2} buried 2 nm below the surface (the center of the dielectric layer), assuming an effective $\kappa=10$. This approximation is valid as long as d+z are small compared to the lateral extent of σ.

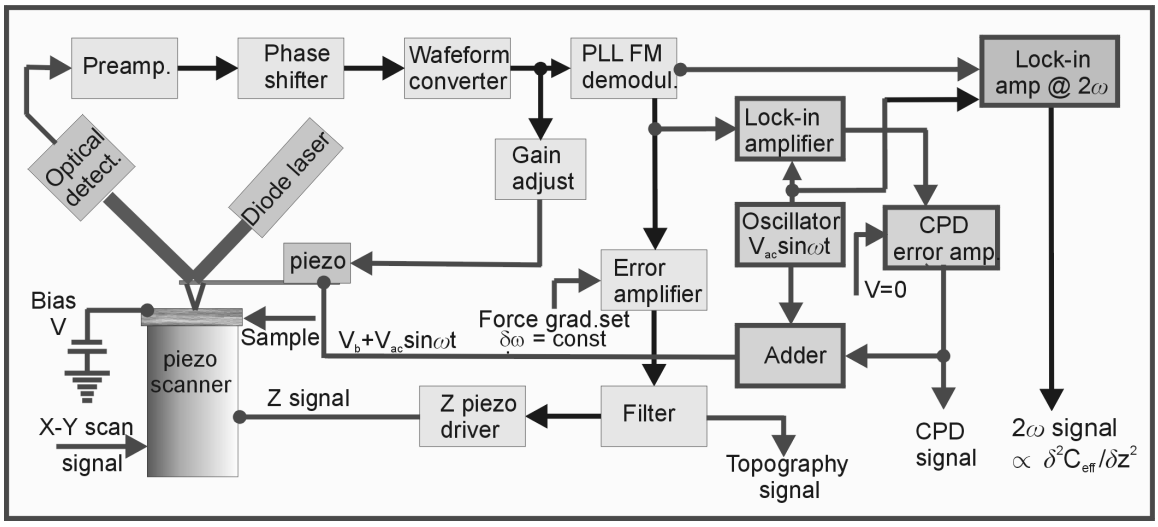

Fig. 1

Schematic of AFM operating in the non-contact mode and showing the three different signal processing (imaging) channels: topography, contact potential difference (CPD) and differential capacitance. The first two are operated under feedback control with constant δω (topography) and $V_b+V_{CPD}=0$ (CPD).

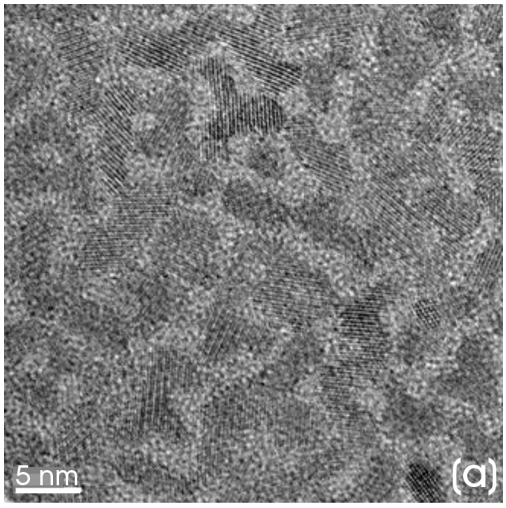

$(HfO_2)_{0.4}(SiO_2)_{0.6}$

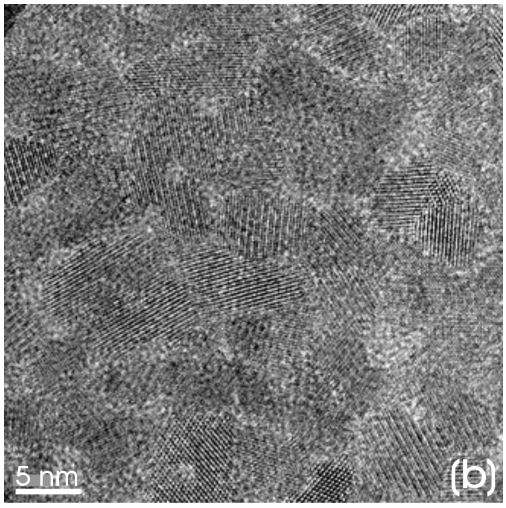

$(HfO_2)_{0.6}(SiO_2)_{0.4}$

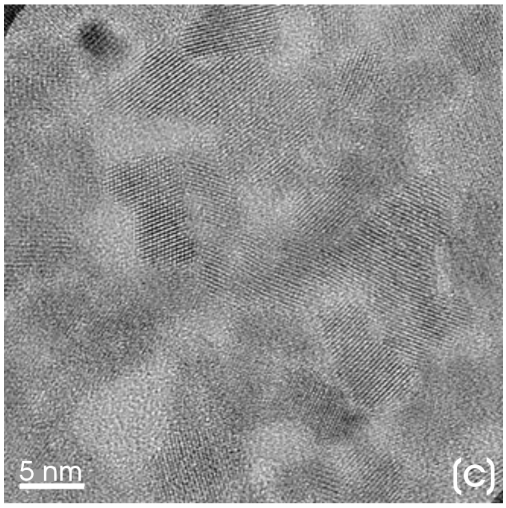

$(HfO_2)_{0.8}(SiO_2)_{0.2}$

Fig. 2: HRTEM images of ~4 nm thick $(HfO_2)_x(SiO_2)_{1-x}$ layers annealed in N_2 at 1000° C for 10 seconds: (a) for x=0.4, (b) for x=0.6 and (c) for x=0.8. Image size is 37×37 nm^2.

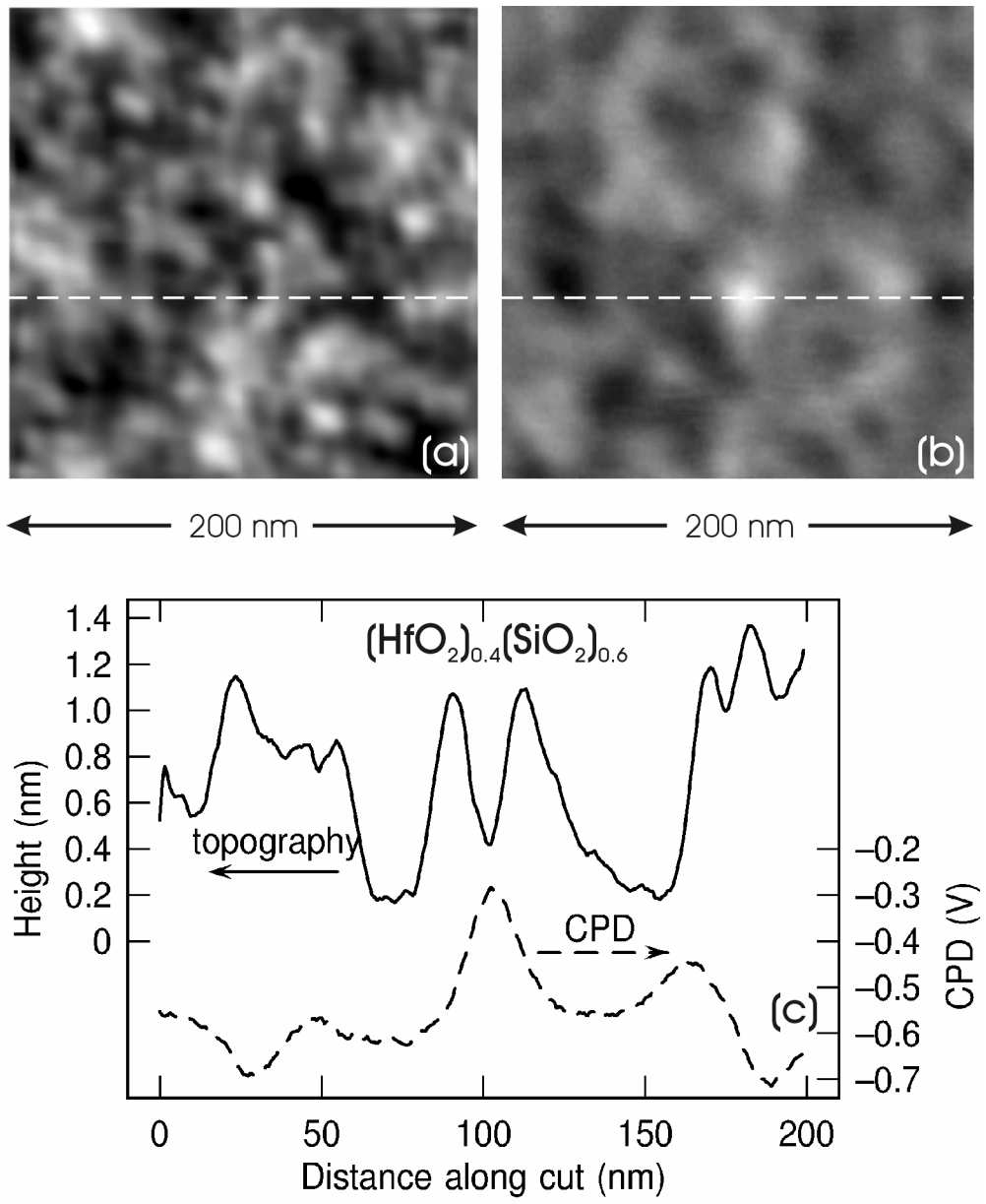

Fig. 3

Topography (a) and simultaneously acquired CPD image (b) of a ~4 nm thick $(HfO_2)_{0.4}(SiO_2)_{0.6}$ layer annealed in N_2 at 1000° C for 10 sec. Dashed lines in images mark the position of the cuts for the profiles shown in (c). Image contrast ranges: (a) 1.97 nm; (b) 0.49 V.

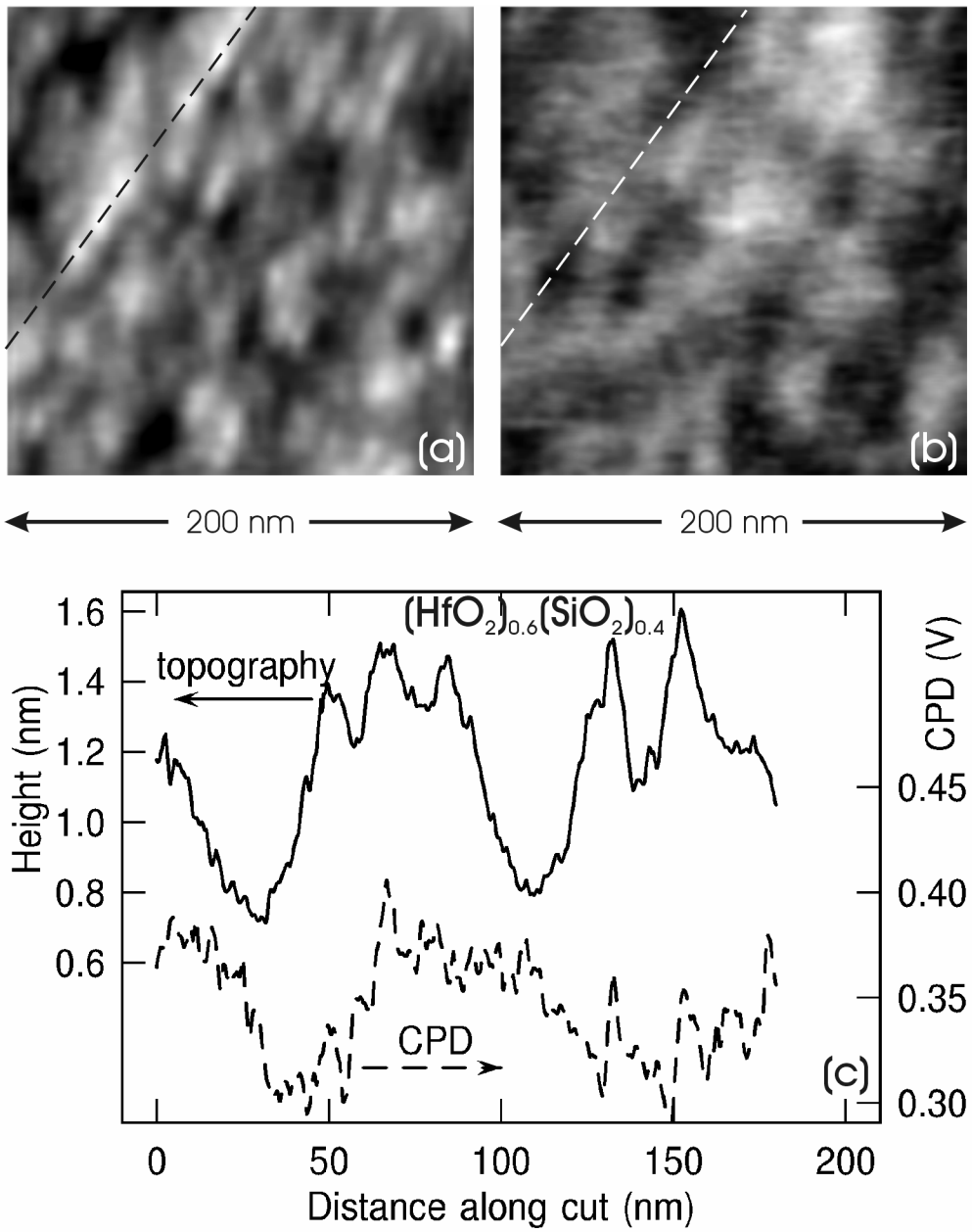

Fig. 4

Topography (a) and simultaneously acquired CPD image (b) of a ~4 nm thick $(HfO_2)_{0.6}(SiO_2)_{0.4}$ layer annealed in N_2 at 1000° C for 10 sec. Dashed lines in images mark the position of cuts for the profiles shown in (c). Image contrast ranges: (a) 1.73 nm; (b) 0.22 V.

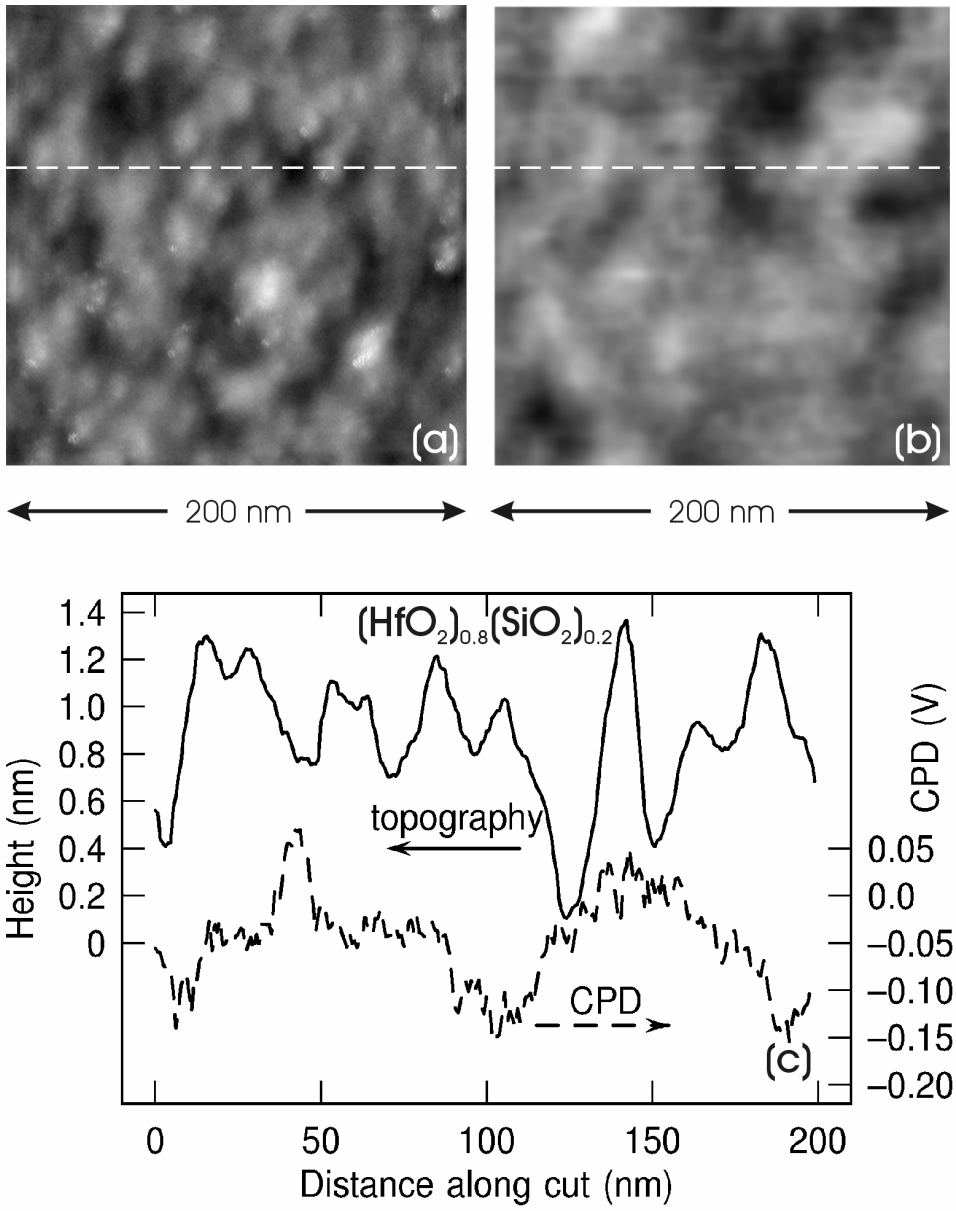

Fig. 5
Topography (a) and simultaneously acquired CPD image (b) of a ~4 nm thick $(HfO_2)_{0.8}(SiO_2)_{0.2}$ layer annealed in N_2 at 1000° C for 10 sec. Dashed lines in images mark the position of cuts for the profiles shown in (c). Image contrast ranges: (a) 2.24 nm; (b) 0.44 V.

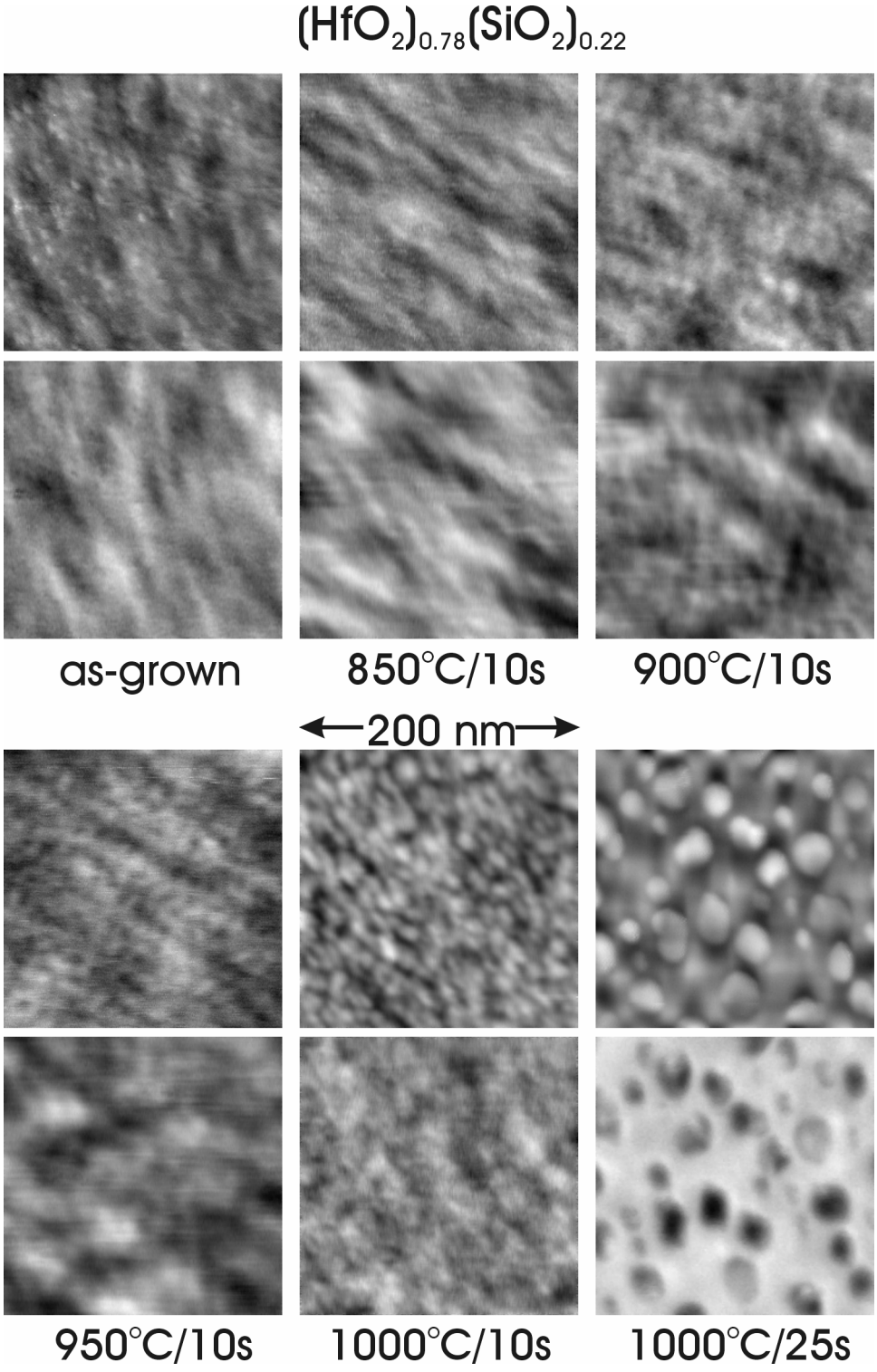

Fig. 6: Topography (top) and CPD images (immediately below) of a sequence of anneals in ultra high vacuum for a 2.2 nm thick $(HfO_2)_{0.78}(SiO_2)_{0.22}$ layer. Image-wide roughness and the CPD range are shown in the graphs of Fig. 7. The topography contrast range is close to twice the mean roughness shown in Fig. 7.

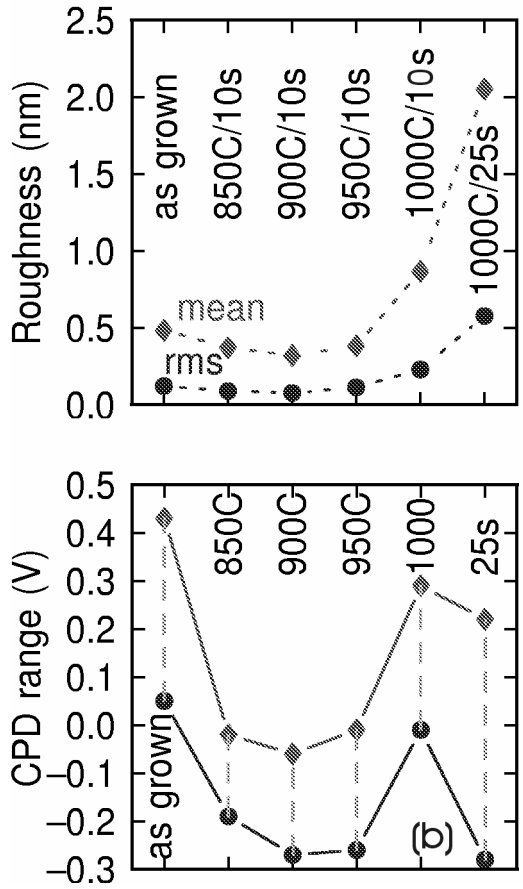

Fig. 7
Mean and rms roughness (a), and CPD range (b) obtained from images in Fig. 6, plotted versus the annealing temperatures.

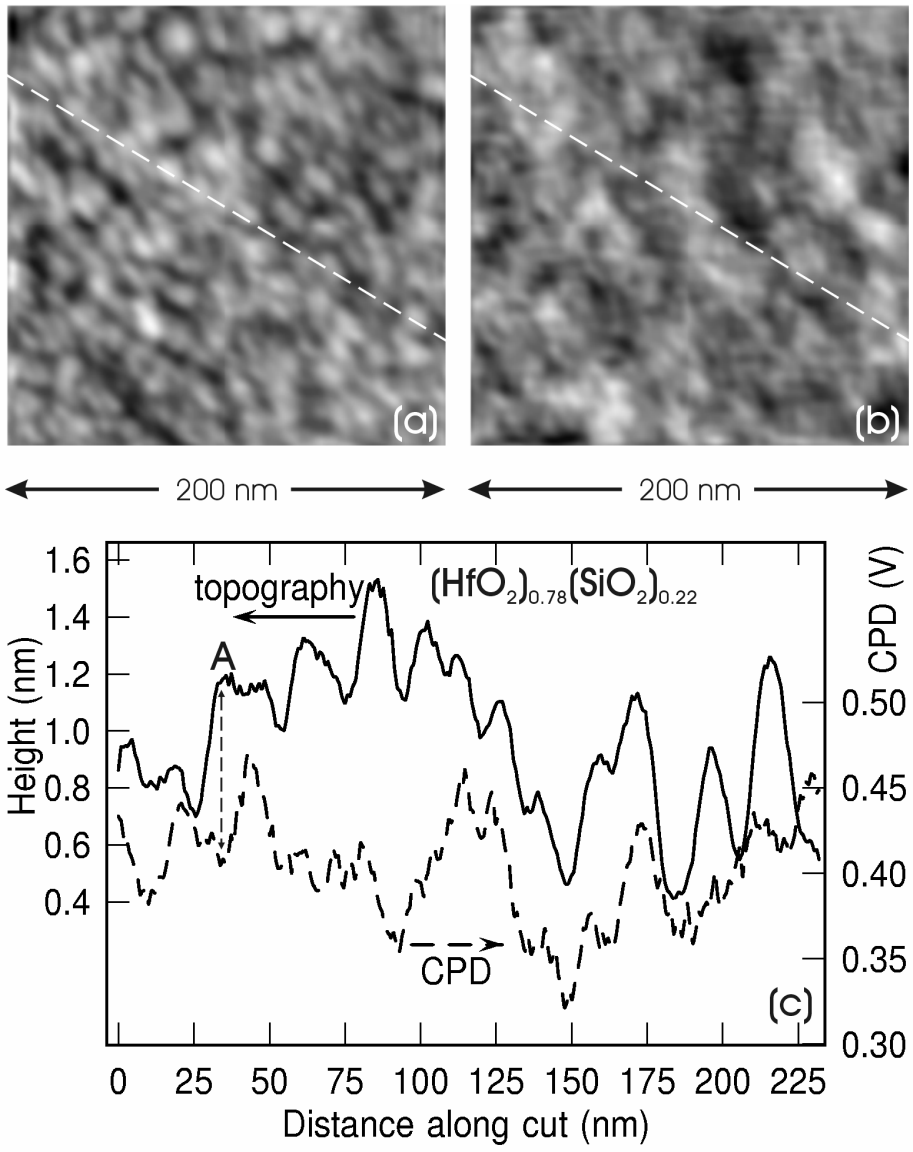

Fig. 8
Topography (a) and simultaneously acquired CPD image (b) of a ~2.2 nm thick $(HfO_2)_{0.78}(SiO_2)_{0.22}$ layer annealed in vacuum at 1000° C for 10 sec. Dashed lines in images mark the position of cuts for the profiles shown in (c). Image contrast ranges: (a) 1.78 nm; (b) 0.30 V.

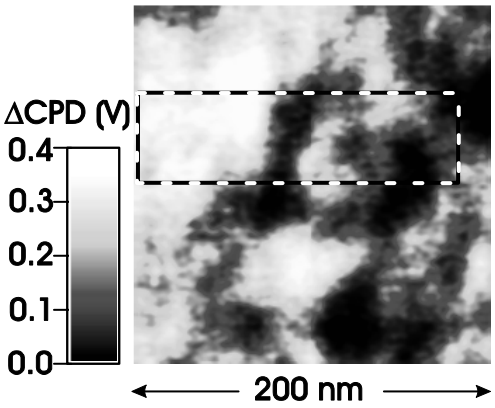

Fig. 9
CPD image of ~4 nm thick $(HfO_2)_{0.8}(SiO_2)_{0.2}$ layer annealed in N_2 at 1000° C for 10 sec. High contrast levels were used to delineate four CPD ranges spaced 0.1 V apart. The rectangle simulates a hypothetical 50 nm gate length region of an active channel placed in an area of potentially detrimental device threshold behavior.